Enhancing Polysulfide Conversion in Lithium–Sulfur Batteries through the Synergistic Effect of 2,6-Dihydroxyanthraquinone and Co Atoms

Huijuan You [a,1], Fangfang Liu[b], Hanxiao Wang[c], Zining Wang[d], Xuyun Wang [a,*], Boshen Zhang[a], Kuanshuo Tang[a], Jianwei Ren [e,*], Rongfang Wang [a,*]

[a] College of Chemical Engineering, Qingdao University of Science and Technology, Qingdao, 266042, China

[b] Shandong Peninsula Blue Economy and Engineering Research Institute, Shandong Engineering Laboratory for Clean Utilization of Chemical Resources, Weifang University of Science and Technology, Shouguang, Weifang, 262700, China

[c] Qingdao Institute of Bioenergy and Bioprocess Technology, Chinese Academy of Sciences, Shandong Energy Institute, Qingdao New Energy Shandong Laboratory, Qingdao 266101, China

[d] School of Chemical Science and Engineer, Tongji University, 1239 Siping Road, Shanghai 200092, China

[e] Department of Chemical Engineering, University of Pretoria, cnr Lynnwood Road and Roper Street, Hatfield 0028, South Africa

*Corresponding author. E-mail address: wangxy@qust.edu.cn (X. Wang); jianwei.ren@up.ac.za (J. Ren); rfwang@qust.edu.cn (R. Wang)

Abstract

Currently, lithium–sulfur batteries for wider applications are challenged by both the shuttle effect in the cathodes as well as the slow kinetics of the sulfur redox reactions. Although metal compounds have been reported to suppress the shuttle effect of lithium polysulfides (LiPSs) by chemically adsorbing LiPSs and catalyzing their conversion, current methods for sulfur fixation on cathode materials remain insufficient. In this work, 2,6-dihydroxyanthraquinone (DHAQ) is tightly adsorbed on a Co-doped porous carbon (Co–C) substrate through π–π stacking. The abundant oxygen-containing functional groups in DHAQ form Li–O bonds with lithium in the LiPSs and enable in situ covalent fixation. Meanwhile, cobalt in Co–C forms Co–S bonds with sulfur in LiPSs, providing an efficient pathway for electron transfer and promoting LiPS conversion. Thus, the DHAQ/Co–C composite provides dual chemical adsorption capabilities that mitigate the "shuttle effect" of LiPSs. Additionally, the conductive merits of the DHAQ and Co–C networks accelerate electron transfer, enhance LiPS redox kinetics, and increase the battery's specific capacity. In the end, the optimized S@DHAQ/Co–C composite demonstrates an initial discharge capacity (1385 mAh g^{-1}) at 0.1C. After 600 cycles, the electrode displays a capacity decay rate of 0.062% at 1C. Compared with metal-based materials that rely solely on chemical sulfur fixation, the synergistic effect of organic oxygen atoms and metals in sulfur fixation offers significant improvements.

Subjects: Adsorption; Batteries; Electrodes; Redox reactions; Sulfur

Keywords: synergistic effect; redox reaction kinetics; molecular orbital energy levels; lithium−sulfur batteries; electron transfer

Synopsis: This study enhances lithium−sulfur battery efficiency through innovative materials, contributing to the advancement of sustainable energy solutions.

1. Introduction

Lithium–sulfur (Li–S) batteries have been widely explored as alternative solutions for energy storage applications because of their high energy storage density and the advantages of cost-effective and environmentally friendly sulfur-active materials. (1−3) However, Li–S batteries face challenges, including slow kinetics in the conversion reaction of sulfur species at the cathode and their shuttle effects, both of which severely limit their commercialization on a large scale. (4−6) Professor Nazar's group reported significant breakthroughs in the specific capacity by utilizing porous carbon as the supporting matrix for sulfur cathodes in Li–S battery assemblies. (7) Despite these advancements, their cycling stability still does not meet commercial application standards because of the poor cycling stability caused by the dissolution of lithium polysulfides (LiPSs) and the shuttle effect in battery electrolytes. (8) In recent years, researchers have developed heterostructures (9−11) and synthesized various highly conductive, large surface area metal–nitrogen-doped carbon materials to modify sulfur cathodes, aiming to adsorb LiPSs and enhance sulfur redox reaction kinetics. (12−16) Li (17) and colleagues applied hollow defective N-doped carbon nanospheres in potassium-ion batteries (PIBs), and the contact curved interfaces (CCIs) created on carbon nanotubes (CNTs) effectively promoted electron transfer and adsorption of K^+ ions. However, metal particles, including individual metal atoms with high free surface energies, tend to aggregate at high loadings. Conversely, in contrast, the reduced quantity of active sites resulting from lower loadings proved inadequate in effectively addressing the diffusion as well as shuttle phenomena associated with polysulfides in lithium–sulfur batteries. (18)

Unlike the variability observed in the types and amounts of active sites within inorganic host materials, organic molecules possess precise molecular structures, providing significant advantages in clarifying their adsorption and catalytic interactions with LiPSs. Specifically, the redox reactions of organic electrode materials are primarily based on electron transfer, which facilitates the promotion of electron transfer in LiPSs. Various organic electrode materials exhibiting redox activity, including organic sulfides, conductive polymers, radical species, and carbonyl-based compounds, have been extensively researched. Out of these, quinone molecules as a subset of carbonyl compounds stand out as highly promising candidates, owing to their strong binding affinity with LiPSs as well as their capacity to enable efficient electron transfer. (19−23) However, the high solubility of quinone molecules in organic electrolytes results in rapid capacity decay, which limits their applicability in liquid batteries. (24) Through leveraging π–π interactions of carbon materials and anthraquinone, Li et al. (25) anchored soluble anthraquinone onto the surface of the carbon substrates. The carbonyl groups in anthraquinone enhance sulfur utilization by forming Li–O bonds with the LiPSs. It is well known that the type, quantity, and position of functional groups in organic molecules are closely related to their redox potentials and catalytic activities. Therefore, rational optimization and design of redox-active centers to balance adsorption and catalytic capabilities are crucial for the development of effective organic electrode materials. (21,26−28) However, most current research primarily focuses on the binding capabilities of functional groups with LiPSs. For instance, Zhang and co-workers (29) explored the binding capabilities of several functional groups (−OH, $–NH_2$, $–OCH_3$, and −COOH) with lithium sulfides (Li_2S_x, where x = 1, 2, 4, 6,

8). Their findings revealed that the −OH group exhibits substantially higher binding energies with Li_2S_4 to Li_2S_8 compared to the other groups, demonstrating its superior ability to suppress the dissolution of LiPSs as well as their shuttle effects in the electrolyte. Fan et al. (30) reported the formation of solid organic polysulfides through the covalent generation of Li–O bonds with LiPSs using −OH groups, which effectively suppressed the shuttle effect. Furthermore, molecular electrostatic potential calculations indicated that carbonyl groups situated at the local minima of the electrostatic potential are more likely to bind lithium. (31) However, there are limited studies on the enhanced catalytic conversion effects of organic molecules after adsorbing LiPSs. Clearly, combining covalent and chemical sulfur fixation methods can improve both the immobilization of polysulfides and their conversion rates in Li–S batteries. By leveraging the potential synergistic effects, it is possible to simultaneously achieve both a high energy density and cycling stability. To date, there have been few reports on the impact of these synergistic effects on enhancing the cycling stability of Li–S batteries.

This study involves the attachment of 2,6-dihydroxyanthraquinone (DHAQ) to Co-doped porous carbon via π–π interactions, with the resulting composite serving as a material for sulfur hosting. The introduction of −OH side groups enhanced the conjugation of DHAQ, which in turn improved π–π interactions with the carbon substrate and also reduced its solubility in the battery electrolyte. Furthermore, hydroxyl groups acted as donors of electrons in increasing the cloud density of electrons on the side of the carbonyl oxygen, which improved its LiPS adsorption capability, formed Li–O bonds, and enabled in situ covalent immobilization. The π–π interactions further increased the molecule's electron cloud density, which sequentially strengthened the adsorption of the LiPSs onto the carbonyl oxygen. Simultaneously, Co atoms chemically anchored LiPSs by forming Co–S bonds, while the adsorption of DHAQ on Co–C enhanced the electronegativity of Co, which allowed the metal to more effectively adsorb LiPSs. Moreover, the conductive profile of the network formed by DHAQ and Co–C accelerated electron transfer and promoted the redox processes of LiPSs. This synergistic effect of both chemical and covalent fixation of sulfur effectively suppressed the shuttle movement of LiPSs, significantly improving the immobilization and conversion rates of LiPSs as well as the Li^+ transport kinetics and reaction. Compared with batteries with only sulfur fixation, those with covalent/chemical sulfur fixation exhibited outstanding capacity and cycling stability. The optimized S@DHAQ/Co–C electrode retained 64% of its initial capacity after 600 cycles at 1C, corresponding to a 0.062% capacity decay rate per cycle.

2. Experimental Section

2.1. Preparation of the Co–C Substrate

To prepare the Co–C substrate, 1 g of peptone together with 0.03 mmol of $Co(NO_3)_2 \cdot 6H_2O$ were dissolved in 2 mL of deionized water. The mixture was sonicated for 5 to 10 min until it was fully dissolved. Subsequently, the solution was placed in a refrigerator and frozen for 12 h to form an ice block. This frozen block was then transferred to a freeze-dryer and lyophilized for 12 h. After drying, the obtained sample, together with 10 g of NaCl, was subjected to ball milling for 3 h at 550 rpm. Following milling, the mixed sample was transferred to a tube furnace and heated to 900 °C at a heating rate of 5 °C min^{-1} under a N_2-protected atmosphere, where it was held at that temperature for 1 h. After cooling, the carbonized product was collected, washed, and dried at 60 °C in an oven.

2.2. Preparation of the DHAQ/Co–C Sample

A 60 mg portion of the Co–C sample was dispersed in 0.05 mM DHAQ solution (20 mL). The mixture was stirred for 30 min before centrifugation. The solid product was then dried for further use.

2.3. Preparation of S@Co–C and S@DHAQ/Co–C Samples

First, the individual Co–C or DHAQ/Co–C samples were mixed with sublimed sulfur (mass ratio of 2:3). The mixture was then ground for 30 min and then transferred to a preheated oven at 155 °C inside a glovebox under argon protection. Sequentially, the S@Co–C and S@DHAQ/Co–C samples were obtained separately after 12 h of the reaction.

2.4. Theoretical Calculations

Density functional theory (DFT) calculations were conducted using the Gaussian 09 software, which incorporates the B3LYP method with the 6-311G(D) basis set as well as the empirical dispersion correction (em = gd3bj). The molecular structures were optimized and verified to ensure the absence of imaginary frequencies. The highest occupied molecular orbital (HOMO) and the lowest unoccupied molecular orbital (LUMO), along with the electrostatic surface potential (ESP), were visualized by Multiwavefn and visual molecular dynamics (VMD).

3. Results and Discussion

In the experiments, a porous Co–C carbon matrix was prepared as substrate by following the procedure reported earlier. (18) As shown in Figure 1a, the carbon substrate adsorbs DHAQ through π–π interactions and renders it insoluble in the electrolyte. Ultraviolet (UV) absorption spectroscopy was used to analyze the molecular structure and interactions between the various molecules and the carbon matrix. The DHAQ solution is shown in Figure 1b and exhibits four distinct UV absorption peaks. The absorption peak observed at 217 nm (Peak I) corresponds to the hydroxyl group, while Peaks II at 252 nm and IV at 325 nm are characteristic of the benzene rings. Peak III at 271 nm is associated with the carbonyl structure. (32) The carbon material employed in this research is a three-dimensional nitrogen-doped carbon network loaded with cobalt (Co–C), as illustrated in Figure S1. Upon dispersing the Co–C material, the UV absorption peaks of the DHAQ solution are markedly reduced until they are entirely eliminated following adsorption onto the carbon matrix. This observation indicates that the π structure of the carbon graphite layers interacts with the π structure of DHAQ through π–π interactions, resulting in the formation of a DHAQ/Co–C composite. Scanning electron microscopy (SEM) images of the Co–C and DHAQ-added samples are shown in Figure S2. Notably, the carbon substrate's overall morphology remains unchanged after adding DHAQ. As seen in Figure 1c, the transmission electron microscopy (TEM) image of the DHAQ/Co–C sample shows a smooth and uniform carbon network surface without any aggregation. This demonstrates that the DHAQ species are uniformly dispersed across the structure of the carbon matrix. Robust binding between DHAQ and the carbon substrate appears to be essential for serving as a functional material for battery cathodes. As illustrated in Figure S3, when DHAQ was suspended in a pure electrolyte, it dissolved in the electrolyte after 7 days. Conversely, the supernatant of the DHAQ/Co–C composite remained colorless, indicating that the binding of DHAQ to the carbon matrix successfully inhibited its solvation in the electrolyte. UV–visible spectroscopy tests were conducted on both the pure electrolyte and the electrolyte containing DHAQ/Co–C after standing for 7 days. As seen in Figure 1d, the UV–visible spectrum of the

electrolyte with DHAQ/Co–C matches that of the pure electrolyte, suggesting that DHAQ did not dissolve in the electrolyte and remained stably adsorbed on Co–C through π–π interactions.

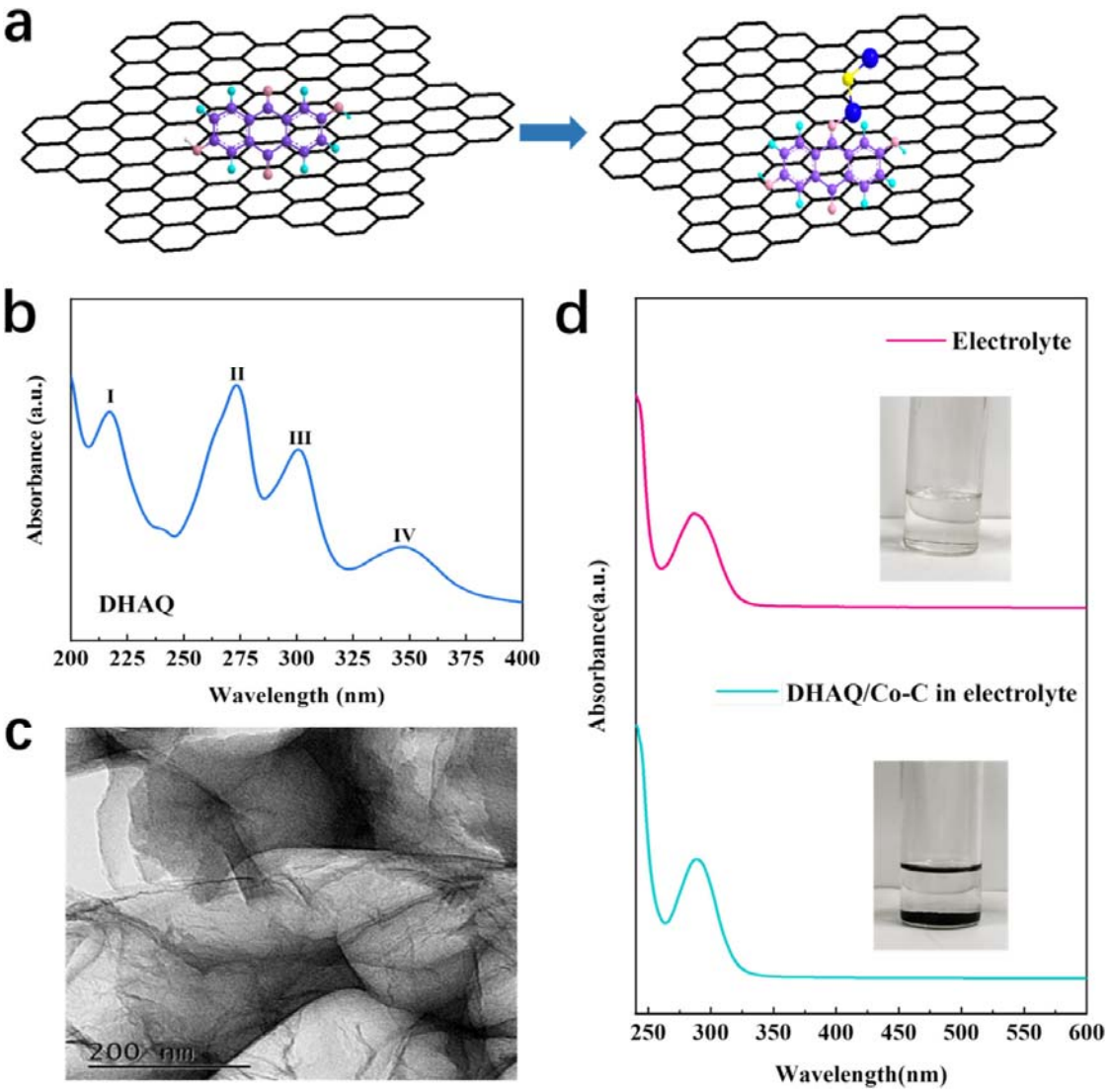

Figure 1. (a) Interaction diagram between DHAQ and LiPSs; (b) UV spectrum of DHAQ; (c) high-resolution TEM image of the DHAQ/Co–C sample; and (d) UV absorption spectra from pure electrolyte as well as electrolyte dispersed with DHAQ/Co–C.

In the experiments, the porous carbon material without Co doping is termed C, and a melt diffusion method was used to load sulfur onto the carbon substrate. The resultant electrode materials are labeled as S@DHAQ/C, S@Co–C, and S@DHAQ/Co–C, respectively. The characteristic XRD peaks of elemental sulfur in orthorhombic crystals are shown in Figure 2a from the multiple diffraction peaks in all three samples (PDF card 08-0247). This indicates that elemental S is distributed uniformly within the carbon support. (33) The SEM images of the S@Co–C and S@DHAQ/Co–C samples are shown in Figure 2b,2c, respectively. Clearly, they reveal the absence of significant sulfur particle aggregation, indicating that the original carbon network structure is retained after sulfur loading. These findings imply that the sulfur element is uniformly loaded across carbon substrates. Additional evidence of this even distribution is also observed in the TEM image in Figure 2d. Furthermore, Figure 2e shows elemental sulfur

mapping within the S@DHAQ/Co–C structure, where the overlapping maps of sulfur and carbon confirm their good dispersion across the sample framework. The optimal DHAQ loading was determined by investigating the cycling stability of different S@DHAQ/Co–C samples at 0.2C with different DHAQ loading contents (Figure S4). It was found that the sample loaded with 0.05 mM DHAQ exhibited the best electrochemical performance. As a small organic molecule, DHAQ possesses both redox activity and the ability to chemically adsorb LiPSs, which effectively suppresses their shuttling effect. Insufficient DHAQ loading leads to weak LiPS adsorption, while excessive loading can result in the aggregation of DHAQ and coverage of co-active sites, thereby reducing the electrocatalytic performance. Therefore, the sample loaded with 0.05 mM DHAQ was selected for further electrochemical studies.

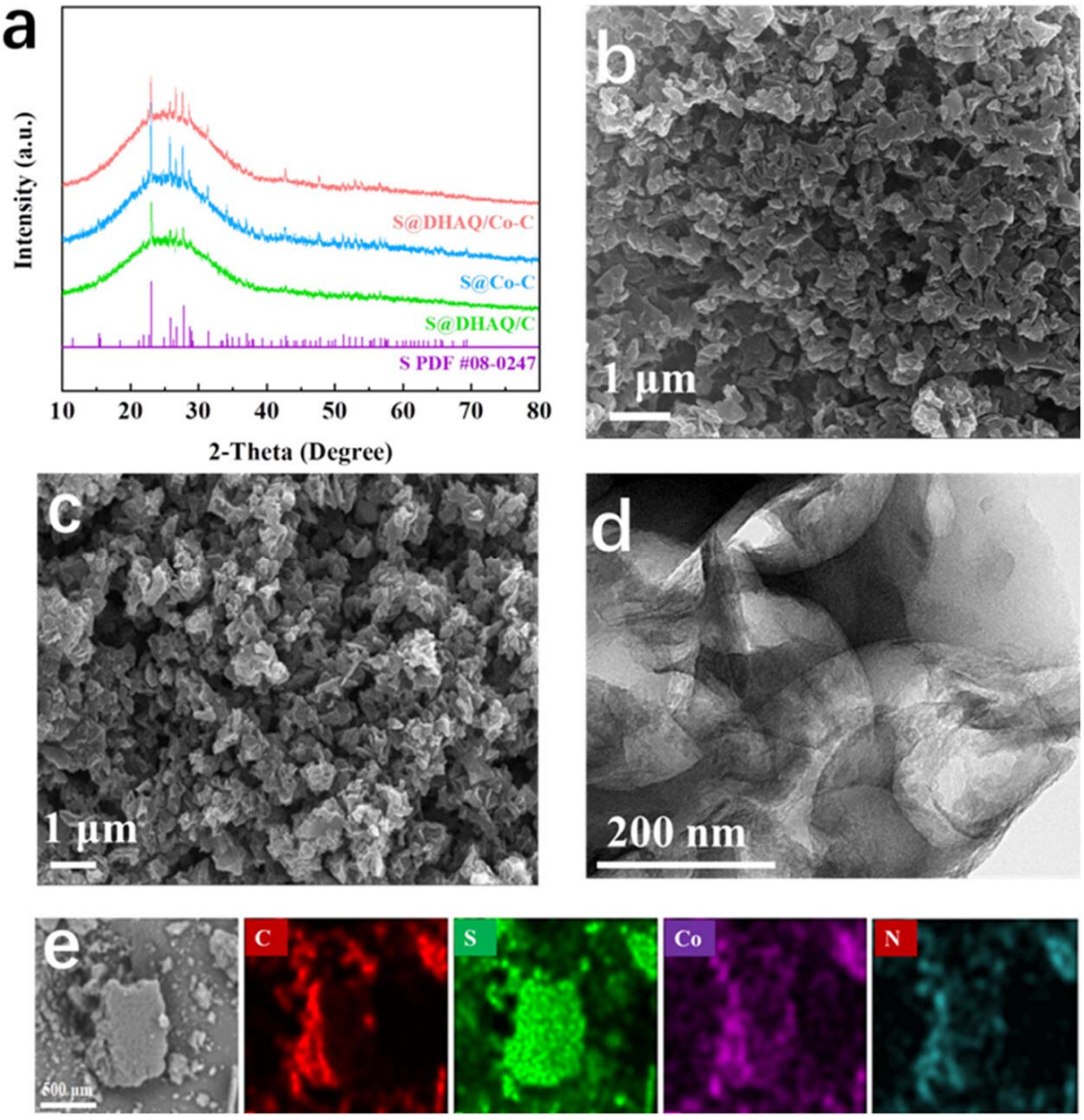

Figure 2. (a) XRD patterns of the prepared samples. SEM images of (b) S@Co–C and (c) S@DHAQ/Co–C samples. (d) TEM image of the S@DHAQ/Co–C sample, as well as (e) the corresponding elemental distributions of S, C, N, and Co.

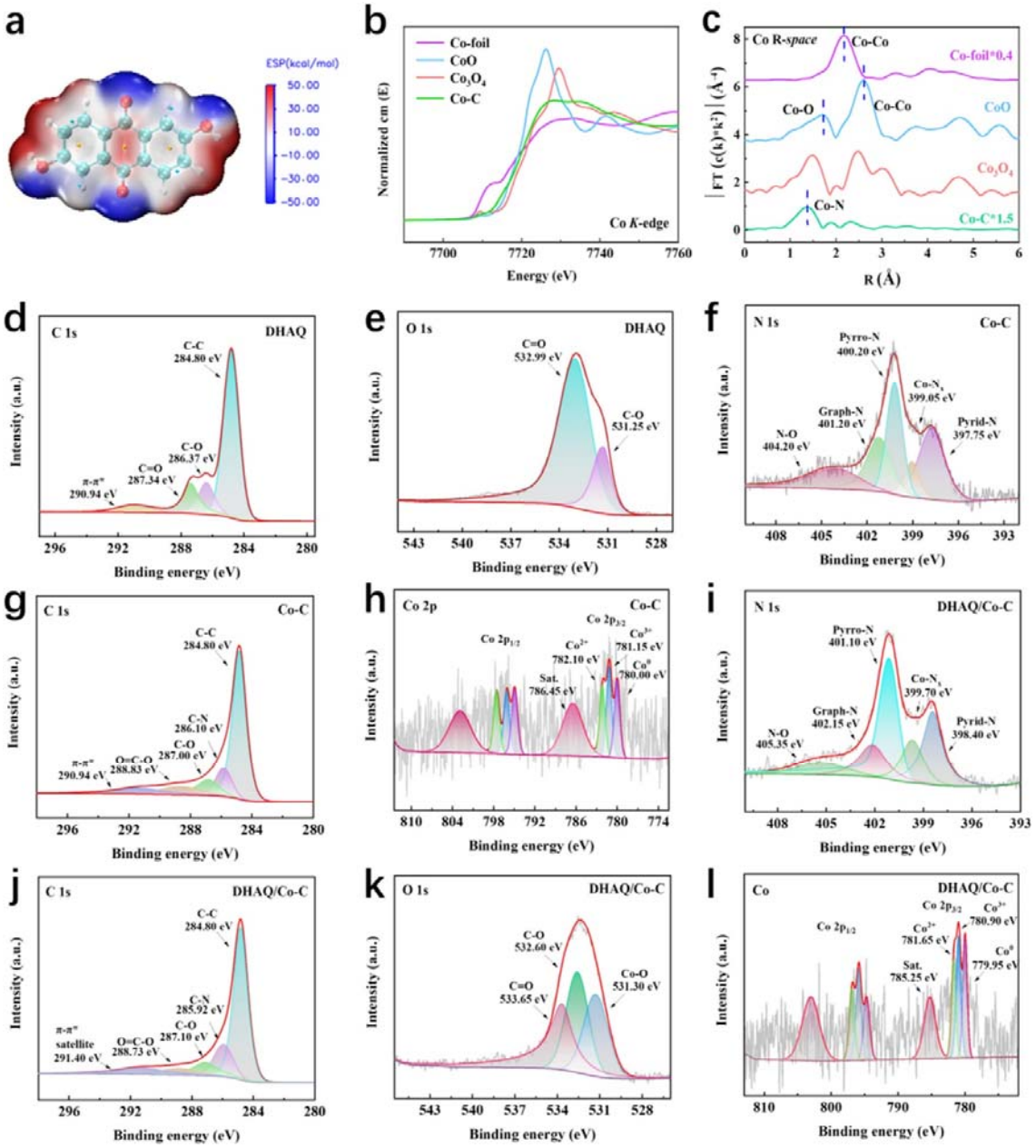

Figure 3. (a) Molecular surface electrostatic potential of the DHAQ sample, (b) Co K-edge XANES of the Co–C sample, and (c) FT-EXAFS of the Co K-edge in R space of the Co–C sample. XPS spectra of the DHAQ sample: (d) C 1s and (e) O 1s. XPS spectra from the Co–C sample: (f) N 1s, (g) C 1s, and (h) Co 2p. XPS spectra of the DHAQ/Co–C sample: (i) N 1s, (j) C 1s, (k) O 1s, and (l) Co 2p.

As reported by Lu et al., molecular surface electrostatic potential (ESP) analysis can be used to investigate the binding ability between various molecules and to identify reactive sites for chemical reactions. (34) As shown in Figure 3a, four local minima in the electrostatic potential of the DHAQ molecule are all located near the oxygen atoms. This indicates that these oxygen atoms are the most probable sites for attracting lithium atoms, which causes the formation of Li–O bonds. (35) Among them, the surface electrostatic potential of the carbonyl oxygen is lower than that of the hydroxyl oxygen, which implies that the carbonyl oxygen preferentially binds to lithium. To probe the binding effect of DHAQ with LiPSs, Co–C and DHAQ/Co–C

samples were placed in a Li_2S_6 solution for 2 h without any disturbance. As illustrated in Figure S5, the solution of Li_2S_6 after adsorption by the DHAQ/Co–C sample shows noticeable discoloration, indicating a strong interaction between the DHAQ/Co–C sample and the LiPS species. As previously reported, (36−38) X-ray absorption fine structure (XAFS) analysis is valuable to disclose the coordination environment as well as the electronic structure of the sample under investigation. As illustrated in Figure 3b, the X-ray absorption near edge structure (XANES) spectrum of the Co–C sample lies between the spectra of the Co foil and Co_3O_4. This finding suggests that the oxidation state of atomically dispersed Co is intermediate, falling between 0 (Co foil) and +2 (CoO). The fitted results in Figure S6 further validate that the valence state of Co in the Co–C sample is between 0 and +2. The Fourier transform extended X-ray absorption fine structure (FT-EXAFS) spectrum of the Co–C sample reveals a distinct peak corresponding to Co–N bonding, located at approximately 1.38 Å (Figure 3c). This finding indicates that both Co and N are doped successfully onto the carbon matrix as stable Co–N bonds. The absence of Co–Co or Co–O peaks confirms that there are no Co clusters or oxides present in the Co–C sample. Collectively, these characterization results validate the successful preparation of a Co and N dual-doped porous carbon network structure. The spectral fitting results of EXAFS in Table S1 indicate that Co has a coordination number of 3.75 within the Co–C sample. These findings demonstrate that Co atoms are dispersed in a $Co–N_4$ configuration within the carbon matrix, with some Co atoms remaining available for bonding with sulfur to form Co–S bonds. This configuration thus facilitates electron transfer and promotes LiPS conversion.

To reveal the synergistic effect of DHAQ and Co atoms in accelerating electron transfer and enhancing the adsorption capacity for LiPSs, X-ray photoelectron spectroscopy (XPS) analyses were performed on the prepared samples. Compared to the original DHAQ sample (287.34 eV, Figure 3d), the binding energy of the C═O group from the DHAQ/Co–C sample shows a shift (288.73 eV, Figure 3j). This confirms that the interaction between DHAQ and the Co–C substrate is primarily based on π–π interactions. (25,39) Figure 3e shows the XPS O 1s spectrum of the DHAQ sample. The two peaks appearing at 531.25 and 532.99 eV belong to the C–O and C═O bonds, respectively. A comparison of the O 1s spectra of the Co–C sample (Figure 3f) and the DHAQ/Co–C sample (Figure 3k) reveals the emergence of a Co–O peak in the DHAQ/Co–C spectrum. This indicates that the oxygen atoms of DHAQ interact with Co after adsorption on the Co–C substrate. Furthermore, the shift in the binding energy of the C═O group to a higher value can be attributed to the increased electron cloud density of DHAQ due to π–π interactions. These interactions contribute to a more stabilized adsorption of DHAQ on the Co–C substrate, as the electron cloud density of the molecule becomes more evenly distributed, thereby lowering its internal energy. The interaction between DHAQ and LiPSs primarily occurs at the carbonyl group, and the increased electron cloud density at this site facilitates its reaction with LiPSs. As observed in Figure 3(f–g), a bond is formed in the Co–C substrate between nitrogen and carbon, where a distinct $Co–N_x$ bond appears at 399.05 eV, which indicates the presence of $Co–N_x$ active species in the Co–C substrate. (40) Previous studies by Dong (41) and Sun (42) have demonstrated that $Co–N_x$ exhibits excellent catalytic activity. The coordination of $Co–N_x$ increases the electronegativity of pyridine and pyrrole nitrogen, thereby enhancing the kinetics of sulfur redox reactions. Another study has shown that pyridine nitrogen improves the catalyst's electrocatalytic performance by creating more defective active sites and facilitating electron transfer during redox reactions. (43) Xiao et al. (44) reported that the stronger interaction between polysulfides and pyrrole nitrogen resulted in higher binding energies. Therefore, nitrogen doping enhanced the polar sites and affinity of the carbon framework for sulfur, which further increased its ability to adsorb LiPSs. In Figure 3i, it can be observed that all the bond binding energies shift toward higher binding energies,

and the increased intensity of the Co–N_x peak suggests that the adsorption of DHAQ strengthens the interaction of Co with LiPSs. The Co 2p spectrum (Figure 3h,I) shows that after the adsorption of DHAQ on the Co–C substrate, the binding energy of Co 2p shifts to a lower binding energy direction. This trend suggests that the electrons from DHAQ tend to shift toward Co and increase the density of the electron cloud around the Co atoms. Subsequently, the enhanced interaction between Co and LiPSs leads to stronger Co–S bonds, which can more effectively adsorb LiPSs.

To reveal the enhancement of catalytic LiPS conversion by the DHAQ/Co–C sample, cyclic voltammetry (CV) curves were obtained to examine the kinetics of redox reactions in Li–S batteries. A typical two-step redox process is shown in Figure 4a for all three electrode samples. The reduction peaks appearing at 2.27 and 2.03 V correspond to reduction processes of $S_8 \rightarrow Li_2S_4 \rightarrow Li_2S$, while the oxidation peaks at 2.34 and 2.39 V are attributed to the reverse processes of $Li_2S \rightarrow Li_2S_4 \rightarrow S_8$. In comparison, the electrode incorporated with S@DHAQ/Co–C exhibits a smaller peak-to-peak separation (355 mV) and a higher peak current density than both the S@Co–C- and S@DHAQ/C-incorporated electrodes. It is well known that the diffusion efficiency of Li^+ ions is a key aspect of the reaction kinetics in Li–S batteries. For instance, slow reaction kinetics can lead to LiPS accumulation in the electrolyte, thereby increasing its viscosity. Figure 4b shows the CV curves of the S@DHAQ/Co–C-incorporated electrode, recorded at different scanning rates. Figures S7 and S8 show the CV curves for the S@Co–C- and S@DHAQ/C-incorporated samples, respectively. By analyzing the shoe CV curves, the Randles–Sevcik equation was used to determine the diffusion coefficient of Li^+ ions (see Supporting Information). (45) Figure 4(c–e) shows the peak currents at different potentials against different scanning rates. The Li^+ diffusion coefficients were determined from the slopes of the linear fitting curves (Table S2). The high Li^+ diffusion coefficients of the S@DHAQ/Co–C sample at various stages indicate that the battery exhibits rapid redox reaction kinetics. Potentiostatic deposition experiments were performed to understand the synergistic effect of DHAQ/Co–C in catalyzing the conversion from soluble Li_2S_x to Li_2S. (46,47) As illustrated in Figure S9, the nucleation capacity of Li_2S on DHAQ/Co–C is the highest (486.6 mAh g^{-1}). Moreover, a shorter nucleation time suggests reduced diffusion of LiPSs and a more efficient catalytic conversion process. Notably, compared to the DHAQ/C and Co–C samples, the DHAQ/Co–C sample exhibits the shortest nucleation time of 3466 s, which implies that the cointeraction between DHAQ and Co greatly promotes nucleation, deposition, and Li_2S catalytic conversion kinetics.

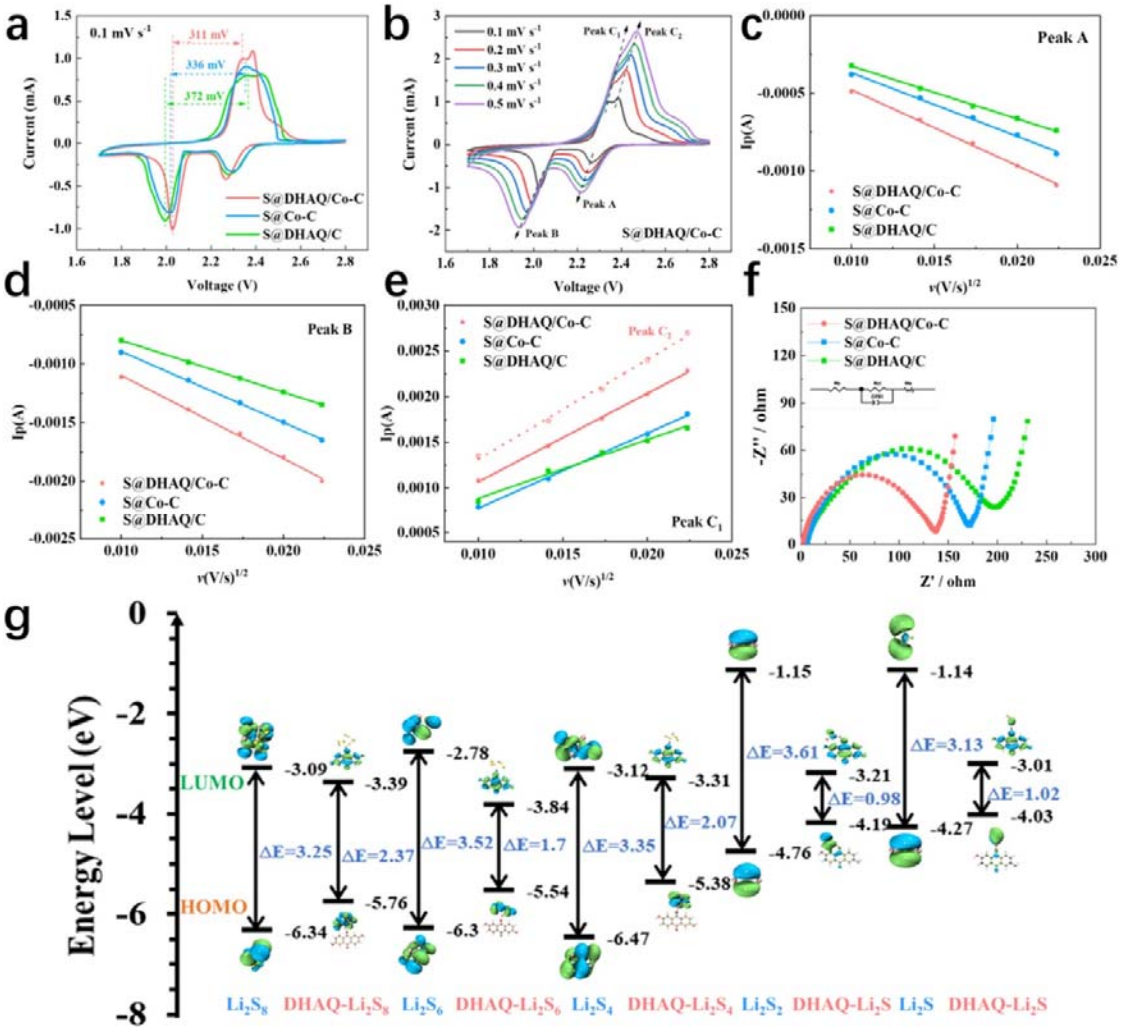

Figure 4. (a) CV curves scanned at 0.1 mV s^{-1} on the S@Co–C and S@DHAQ/Co–C samples, (b) CV curves scanned at 0.1–0.5 mV s^{-1} on the S@DHAQ/Co–C sample, (c–e) linear fitting results of current peaks from the three samples, (f) electrochemical impedance spectra of the three samples, and (g) a schematic illustration depicting the energy levels from several DHAQ-Li_2S_x complexes, highlighting their electronic interactions and energy alignment.

Further, electrochemical impedance spectra (EIS) were recorded to reveal the cooperative action of DHAQ and Co atoms on the interfacial reaction processes. As seen in Figure 4f, the semicircle observed at high frequencies is associated with the charge transfer resistance. In the high-frequency region, a smaller impedance value exhibited by the S@DHAQ/Co–C-incorporated sample indicates that the cooperative action of DHAQ and Co atoms promotes the rapid redox reactions of LiPSs, resulting in improved reaction kinetics. In the low-frequency region, the slope reflects the ionic diffusion resistance, with the S@DHAQ/Co–C-incorporated sample demonstrating the lowest resistance to ionic diffusion. This indicates that the cooperative action of DHAQ and Co atoms facilitates the charge transfer rate at the electrode's interfacial surface while accelerating the ionic diffusion kinetics within the electrode. In principle, the redox behavior of a compound is closely related to the energy levels of its frontier molecular orbitals. A higher HOMO energy indicates that a compound can more readily lose electrons, signifying a stronger reducing ability as a reductant. Conversely, a lower LUMO energy corresponds to a greater oxidizing ability. (48,49) As shown in Figure 4g, the

frontier molecular orbital energy levels of Li_2S_x and DHAQ-Li_2S_x were calculated to assess the promoting effect of DHAQ on the redox reaction kinetics of the polysulfides. In contrast, the higher HOMO energy and lower LUMO energy of DHAQ-Li_2S_x suggest that DHAQ-Li_2S_x is not only more likely to accept electrons as an oxidant during the discharge process but also more likely to lose electrons as a reductant during the charging process. Given the HOMO (−5.54 eV) and LUMO (−3.84 eV) energies of DHAQ-Li_2S_6, the increase by 0.76 eV in HOMO energy suggests a more ready oxidization to S_8 during the charging process, while the decrease by 1.06 eV in LUMO energy suggests an easier reduction to Li_2S during the discharging process. This theoretically demonstrates that DHAQ participation in the fixation of Li_2S_x can catalyze the bidirectional conversion of LiPSs, and thereby accelerate the kinetics of the Li_2S_x redox reaction.

Provided that DHAQ can immobilize LiPSs and catalyze their conversion, the performance advantages of the S@DHAQ/Co–C-incorporated electrode for the cycling stability of Li–S batteries were further assessed. To rule out the partial contribution of DHAQ to the storage capacity during the charge–discharge process, a lithium foil anode and DHAQ/Co–C as a sulfur-free cathode were used to assemble the battery. As shown in Figure S10, the capacity provided by DHAQ is minimal (0.006 mAh) and can therefore be neglected. From the thermogravimetric (TGA) analysis in Figure S11, the sulfur loading on the carbon substrate was calculated as 59.77 wt %, and the battery capacity was determined from the actual sulfur-loading content. Figure 5a shows the charge–discharge curves of the first cycle at 0.1C for the three electrode samples. In contrast, the initial discharge capacity of the S@DHAQ/Co–C-incorporated electrode sample (1385 mAh g^{-1}) is larger than that of the S@Co–C-incorporated electrode (1162 mAh g^{-1}) and S@DHAQ/C-incorporated electrode (1123 mAh g^{-1}). In addition to capacity, the voltage distribution (ΔE) and the Q_L/Q_H ratio between low discharge platform capacity (Q_L) and high discharge platform capacity (Q_H) also serve as an important index for assessing the performance of a battery. (50) As shown in Figure 5b, the lower ΔE (203 mV) and the higher Q_L/Q_H ratio (2.98) from the S@DHAQ/Co–C-incorporated sample indicate that the combined effect of DHAQ and Co facilitates the catalytic LiPS conversion while accelerating the process of solid–liquid–solid conversion. Figure 5c,d show the cycling stabilities of the two electrode samples at current densities of 0.2 and 1C, respectively. An initial discharge capacity of 1009 mAh g^{-1} is delivered by S@DHAQ/Co–C-incorporated electrode at 0.2C. After 120 cycles, the sample displays a minimal capacity decay rate of 0.19% per cycle. The decay rate appears to be even lower at 1C, at just 0.062% per cycle over 600 cycles. In comparison to previously reported results, the electrode incorporated with the S@DHAQ/Co–C sample exhibits good cycling stability over those electrodes incorporated with other materials (Table S3). These findings indicate that the synergistic effect of DHAQ and Co significantly improved the cycling stability of Li–S batteries. Moreover, the rate performances of the three electrode samples were evaluated at various current densities. As presented in Figure 5e, the electrode incorporated with S@DHAQ/Co–C exhibits an individual discharge capacity of 1174 mAh g^{-1} at 0.1C, 774 mAh g^{-1} at 0.2C, 674 mAh g^{-1} at 0.5C, 596 mAh g^{-1} at 1C, and 475 mAh g^{-1} at 2C. After setting the current density back to 0.2C, the discharge capacity of the S@DHAQ/Co–C-incorporated electrode reached 730 mAh g^{-1}, maintaining 94.3% of its initial discharge capacity. Figure 5f displays the profiles of the S@DHAQ/Co–C sample during charging–discharging at various current densities. These curves indicate that during high-current discharge, the sample achieves a high discharge capacity and also retains the characteristic charging–discharging features of a typical battery. In comparison, the samples incorporated with S@Co–C and S@DHAQ/C exhibit greater polarization, as shown in Figures S12 and S13, respectively. The smaller polarization observed in the S@DHAQ/Co–C sample suggests that the combined effect of DHAQ and Co

significantly accelerates the redox reaction of sulfur. In addition, the cycling stability of the S@DHAQ/Co–C electrode was evaluated at 0.2 C and the loaded sulfur amounts are 3.5 mg cm^{-2} (E/S = 8 μL mg^{-1}) and 5.0 mg cm^{-2} (E/S = 6 μL mg^{-1}), respectively. As seen in Figure S14, the initial discharge capacities are 779 and 661 mAh g^{-1}, respectively, with a slight capacity degradation rate of 0.49 and 0.40% per cycle following 100 cycles. These observations suggest that the S@DHAQ/Co–C electrode maintains a high discharge capacity as well as excellent cycling stability even at high sulfur loadings, suggesting a significant synergistic effect between DHAQ and Co–C. These results clearly demonstrate that the combined action of DHAQ and Co improves LiPS adsorption, accelerates the kinetics of redox reactions, and ultimately enhances sulfur utilization.

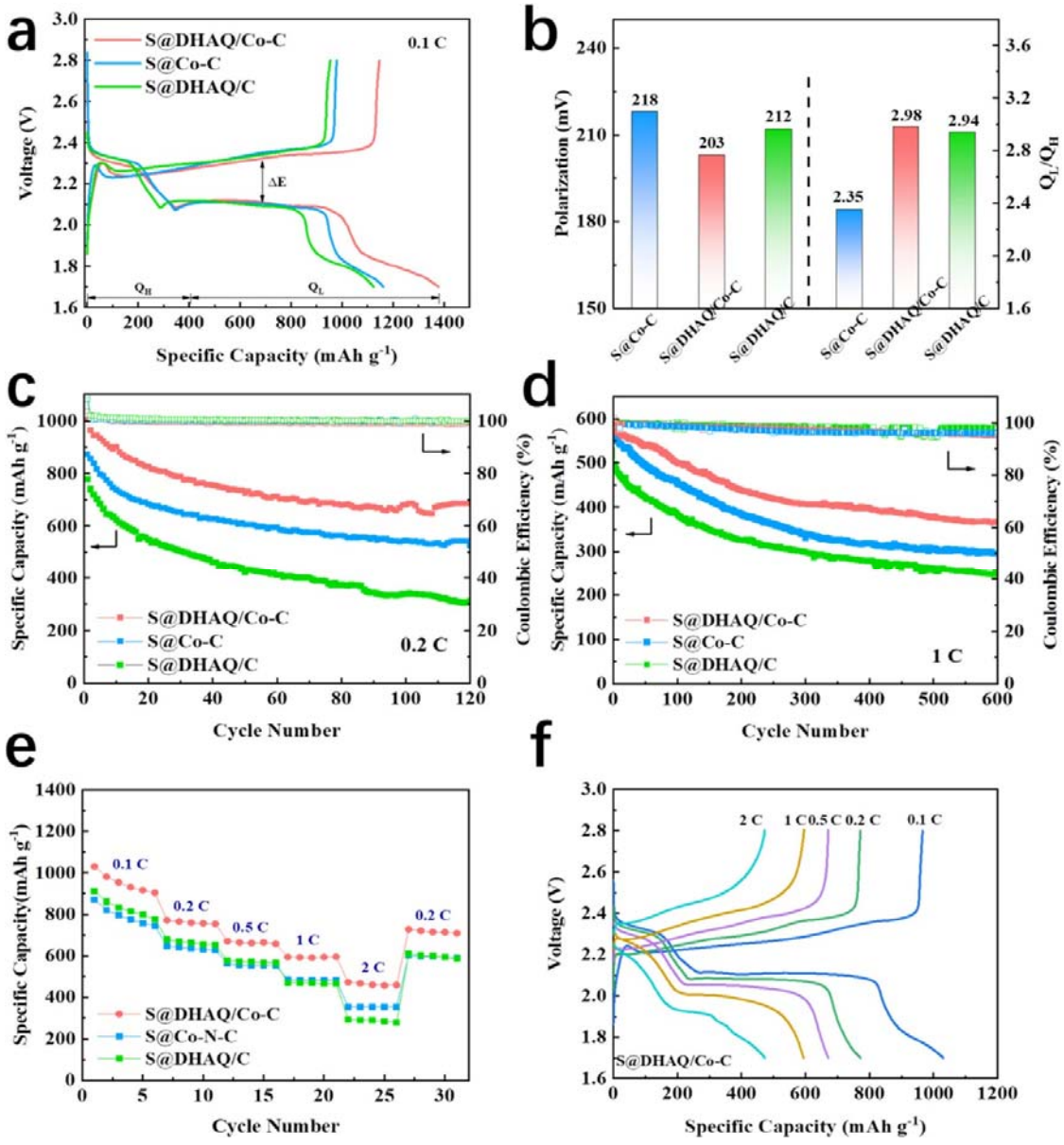

Figure 5. Cycling tests of the prepared samples: (a) charge–discharge curves of the 1st cycle at a rate of 0.1C, (b) calculated values of Q_L/Q_H and polarization (ΔE). Cycling stabilities of the prepared samples at rates of (c) 0.2 and (d) 1C. (e) Rate performance of the prepared samples and (f) charge–discharge curves recorded at various current densities on the S@DHAQ/Co–C-incorporated sample.

4. Conclusions

In summary, an efficient sulfur electrode was developed by combining an organic small-molecule DHAQ with Co–C materials. This provides physical confinement and robust dual chemical adsorption capability for lithium-ion polysulfides (LiPSs). In the charge–discharge process, DHAQ effectively covalently immobilizes LiPSs by forming Li–O bonds with them. The π–π interactions between DHAQ and Co–C increase the electron cloud density of DHAQ and sequentially enhance its adsorption capacity for LiPSs. Additionally, the Co–C substrate accommodates more sulfur and mitigates volume changes during charging and discharging. The Co–S bonds formed with LiPSs facilitate further chemical adsorption. Under the influence of DHAQ, the electronegativity of cobalt is enhanced, which enables more effective fixation of LiPSs and inhibits their diffusion into the electrolyte. Moreover, the conductive matrix constructed by DHAQ and Co–C accelerates electron transfer, promotes the redox reactions of LiPSs, and increases the specific capacity of lithium–sulfur (Li–S) batteries.

These characteristics impart exceptional electrochemical performance to the S@DHAQ/Co–C composite. Electrostatic potential (ESP) calculations indicate that hydroxyl and carbonyl oxygens act as potential adsorption sites for LiPSs, primarily because the O atoms on the DHAQ molecule form Li–O bonds that covalently immobilize the LiPSs. Frontier molecular orbital theory calculations reveal that the complex formed between DHAQ and LiPSs exhibits a higher HOMO energy and a lower LUMO energy, indicating stronger redox activity and faster kinetics of LiPS conversion. Lastly, the optimized S@DHAQ/Co–C sample at 0.2C achieved an impressive discharge capacity (1009 mAh g^{-1}). After 120 cycling tests, the sample exhibited a minimal capacity decay rate of 0.19% per cycle. Additionally, a remarkably low decay rate in the storage capacity (0.062% per cycle) at 1C was also achieved after 600 cycles. The synergistic effect arising from covalent and chemical sulfur fixation offers a novel approach to the development of high-performance electrode materials.

Acknowledgments

The financial support for this work is gratefully acknowledged, with thanks to a research grant (ZR2022MB118) from the Natural Science Foundation of Shandong Province, China.

References

1. Li, H.; Yang, H.; Ai, X. Routes to electrochemically stable sulfur cathodes for practical Li-S batteries. *Adv. Mater.* **2023**, 2305038 DOI: 10.1002/adma.202305038
2. Shao, Q.; Zhu, S.; Chen, J. A review on lithium-sulfur batteries: challenge, development, and perspective. *Nano Res.* **2023**, *16*, 8097–8138, DOI: 10.1007/s12274-022-5227-0
3. Liu, Z.; Chen, M.; Zhou, D.; Xiao, Z. Scavenging of ″dead sulfur″ and ″dead lithium″ revealed by integrated-heterogeneous catalysis for advanced lithium-sulfur batteries. *Adv. Funct. Mater.* **2023**, *33* (46), 2306321 DOI: 10.1002/adfm.202306321
4. Guo, J.; Jiang, H.; Li, X.; Chu, Z.; Zheng, W.; Dai, Y.; Jiang, X.; Wu, X.; He, G. Defective graphene coating-induced exposed interfaces on CoS nanosheets for high redox electrocatalysis in lithium-sulfur batteries. *Energy Storage Mater.* **2021**, *40*, 358– 367, DOI: 10.1016/j.ensm.2021.05.031
5. Wu, Y.-J.; Chen, C.-H.; Lin, S.-H.; Huang, C.-L.; Yeh, Y.-X.; Tan, J.-Y.; Su, J.-T.; Hsieh, C.-T.; Lu, S.-Y. Trip le functionalization of carved N-doped carbon nanoboxes

with synergistic trimetallic sulphide for high performance lithium-sulphur batteries. *J. Mater. Chem. A* **2021**, *9*, 9028– 9037, DOI: 10.1039/D1TA00077B
6. Du, B.; Luo, Y.; Yang, Y.; Xue, W.; Liu, G.; Li, J. COFs-confined multifunctional sulfur-host design towards high-performance lithium-sulfur batteries. *Chem. Eng. J.* **2022**, *442*, 135823, DOI: 10.1016/j.cej.2022.135823
7. Ji, X.; Lee, K. T.; Nazar, L. F. A highly ordered nanostructured carbon-sulphur cathode for lithium-sulphur batteries. *Nat. Mater.* **2009**, *8*, 500–506, DOI: 10.1038/nmat2460
8. Zeng, P.; Peng, J.; Yu, H.; Zhou, X.; Wang, K.; Liu, J.; Zhou, Z.; Chen, M.; Miao, C.; Guo, X.; Chang, B.; Wang, X. In-situ synthesis of highly graphitized and Fe/N enriched carbon tubes as catalytic mediums for promoting multi-step conversion of lithium polysulfides. *Carbon* **2022**, *192*, 418– 428, DOI: 10.1016/j.carbon.2022.02.045
9. Eric, G.; Ma, C.; Kincaid, G.; Angel, C.; Hou, D.; Xiong, H. Heterostructure engineering in electrode materials for sodium-ion batteries: Recent progress and perspectives. *eScience* **2023**, *3*, 100139 DOI: 10.1016/j.esci.2023.100139
10. Wang, M.; Lv, S.; Li, M.; Li, X.; Li, C.; Li, Z.; Chen, X.; Wu, J.; Li, X.; Chen, Y.; Chen, Q. A heterogeneous quasi-solid-state hybrid electrolyte constructed from electrospun nanofibers enables robust electrode/electrolyte interfaces for stable lithium metal batteries. *Adv. Fiber Mater.* **2024**, *6*, 727– 738, DOI: 10.1007/s42765-023-00371-8
11. Chen, H.; Wu, J.; Li, M.; Zhao, J.; Li, Z.; Wang, M.; Li, X.; Li, C.; Chen, X.; Li, X.; Mai, Y.-W.; Chen, Y. Heterogeneous structure design for stable Li/Na metal batteries: Progress and prospects. *eScience* **2025**, *5*, 100281 DOI: 10.1016/j.esci.2024.100281
12. Feng, T.; Zhao, T.; Zhang, N.; Duan, Y.; Li, L.; Wu, F.; Chen, R. 2D amorphous Mo-doped CoB for bidirectional sulfur catalysis in lithium sulfur batteries. *Adv. Funct. Mater.* **2022**, *32*, 2202766 DOI: 10.1002/adfm.202202766
13. Qin, B.; Zhao, X.; Wang, Q.; Yao, W.; Cai, Y.; Chen, Y.; Wang, P.; Zou, Y.; Cao, J.; Zheng, X.; Qi, J.; Cai, W. A tandem electrocatalyst with dense heterointerfaces enabling the stepwise conversion of polysulfide in lithium-sulfur batteries. *Energy Storage Mater.* **2023**, *55*, 445– 454, DOI: 10.1016/j.ensm.2022.12.014
14. Song, X.; Tian, D.; Qiu, Y.; Sun, X.; Jiang, B.; Zhao, C.; Zhang, Y.; Xu, X.; Fan, L.; Zhang, N. Efficient polysulfide trapping and conversion on N-doped $CoTe_2$ via enhanced dual-anchoring effect. *Small* **2021**, *17*, 2102962 DOI: 10.1002/smll.202102962
15. Wang, L.; Shi, H.; Xie, Y.; Wu, Z.-S. Boosting solid–solid conversion kinetics of sulfurized polyacrylonitrile via MoS_2 doping for high-rate and long-life Li-S batteries. *Carbon Neutralization* **2023**, *2*, 262– 270, DOI: 10.1002/cnl2.61
16. Li, C.; Tong, L.; Wang, S.; Liu, Q.; Wang, Y.; Li, X.; Wang, M.; Li, M.; Chen, X.; Wu, J.; Chen, Q.; Mai, Y.; Fan, W.; Chen, Y.; Li, X. Nitrogen doping induced by intrinsic defects of recycled polyethylene terephthalate-derived carbon nanotubes. *SusMat* **2023**, *3*, 431– 440, DOI: 10.1002/sus2.140
17. Li, X.; Wang, Y.; Wu, J.; Tong, L.; Wang, S.; Li, X.; Li, C.; Wang, M.; Li, M.; Fan, W.; Chen, X.; Chen, Q.; Wang, G.; Chen, Y. Engineering contact curved interface with high-electronic-state active sites for high-performance potassium-ion batteries. *Proc. Natl. Acad. Sci. U.S.A.* **2023**, *120*, 2307477120 DOI: 10.1073/pnas.2307477120
18. Zhang, F.; Ji, S.; Wang, H.; Liang, H.; Wang, X.; Wang, R. Implanting cobalt atom clusters within nitrogen-doped carbon network as highly stable cathode for lithium-sulfur batteries. *Small Methods* **2021**, *5*, 2100066, DOI: 10.1002/smtd.202100066

19. Han, C.; Li, H.; Shi, R.; Zhang, T.; Tong, J.; Li, J.; Li, B. Organic quinones towards advanced electrochemical energy storage: recent advances and challenges. *J. Mater. Chem. A* **2019**, *7*, 23378– 23415, DOI: 10.1039/C9TA05252F
20. Son, E. J.; Kim, J. H.; Kim, K.; Park, C. B. Quinone and its derivatives for energy harvesting and storage materials. *J. Mater. Chem. A* **2016**, *4*, 11179– 11202, DOI: 10.1039/C6TA03123D
21. Huang, G.; Jia, K.; Li, X.; Zhang, J.; Luo, Y.; Zhong, C.; Zhu, L.; Wu, F. Modifying rGO with multicarbonyl organic molecule for lithium sulfur batteries with high performance. *Appl. Surf. Sci.* **2023**, *615*, 156430 DOI: 10.1016/j.apsusc.2023.156430
22. Lau, K.-C.; Shkrob, L. A.; Rago, N. L. D.; Connell, J. G.; Phelan, D.; Hu, B.; Zhang, L.; Zhang, Z.; Liao, C. Improved performance through tight coupling of redox cycles of sulfur and 2,6-polyanthraquinone in lithium-sulfur batteries. *J. Mater. Chem. A* **2017**, *5*, 24103– 24109, DOI: 10.1039/C7TA08129D
23. Zhang, W.; Ma, F.; Wu, Q.; Cai, Z.; Zhong, W.; Zeng, Z.; Cheng, S.; Xie, J. Bifunctional fluorinated anthraquinone additive for improving kinetics and interfacial chemistry in rechargeable Li-S batteries. *ACS Appl. Energy Mater.* **2022**, *5*, 15719– 15728, DOI: 10.1021/acsaem.2c03306
24. Lu, Y.; Chen, J. Prospects of organic electrode materials for practical lithium batteries. *Nat. Rev. Chem.* **2020**, *4*, 127– 142, DOI: 10.1038/s41570-020-0160-9
25. Li, G.; Wang, X.; Seo, M. H.; Li, M.; Ma, L.; Yuan, Y.; Wu, T.; Yu, A.; Wang, S.; Lu, J.; Chen, Z. Chemisorption of polysulfides through redox reactions with organic molecules for lithium-sulfur batteries. *Nat. Commun.* **2018**, *9*, 705 DOI: 10.1038/s41467-018-03116-z
26. Zhou, J.; Qian, S.; Hao, B.; Liu, J.; Zhou, X.; Yan, C.; Qian, T. Small molecules, great powers: chemistry of small organo-chalcogenide molecules in rechargeable Li-sulfur batteries. *Adv. Funct. Mater.* **2023**, *33*, 2213966 DOI: 10.1002/adfm.202213966
27. Liu, J.; Xue, M.; Zhou, Y.; Liu, S.; Yan, T. Effective chemisorption of polysulfides through organic molecules for high-performance lithium-sulfur batteries. *Chem. Eng. J.* **2023**, *459*, 141556 DOI: 10.1016/j.cej.2023.141556
28. Xiao, Y.; Xiang, Y.; Guo, S.; Wang, J.; Ouyang, Y.; Li, D.; Zeng, Q.; Gong, W.; Gan, L.; Zhang, Q.; Huang, S. An ultralight electroconductive metal-organic framework membrane for multistep catalytic conversion and molecular sieving in lithium-sulfur batteries. *Energy Storage Mater.* **2022**, *51*, 882– 889, DOI: 10.1016/j.ensm.2022.07.018
29. Zhang, J.; Yang, J.; Liu, Z.; Zheng, B. Interaction mechanisms between lithium polysulfides/sulfide and small organic molecules. *ACS Omega* **2021**, *6*, 4995– 5000, DOI: 10.1021/acsomega.0c06067
30. Fan, X.; Yuan, R.; Lei, J.; Lin, X.; Xu, P.; Cui, X.; Cao, L.; Zheng, M.; Dong, Q. Turning soluble polysulfide intermediates back into solid state by a molecule binder in Li-S batteries. *ACS Nano* **2020**, *14*, 15884– 15893, DOI: 10.1021/acsnano.0c07240
31. Feng, M.; Zeng, R.; Chou, S.-L.; Gu, F. L. Enhancing the understanding of the redox properties of lithium-inserted anthraquinone derivatives by regulating molecular structure. *J. Electroanal. Chem.* **2021**, *887*, 115172 DOI: 10.1016/j.jelechem.2021.115172
32. Yang, J.; Wang, Z.; Shi, Y.; Sun, P.; Xu, Y. Poorly soluble 2,6-Dimethoxy-9,10-anthraquinone cathode for lithium-ion batteries: the role of electrolyte concentration. *ACS Appl. Mater. Interfaces* **2020**, *12*, 7179– 7185, DOI: 10.1021/acsami.9b19623
33. Wang, P.; Zeng, R.; You, L.; Tang, H.; Zhong, J.; Wang, S.; Yang, T.; Liu, J. Graphene-like matrix composites with Fe_2O_3 and Co_3O_4 as cathode materials for

lithium-sulfur batteries. *ACS Appl. Nano Mater.* **2020**, *3*, 1382– 1390, DOI: 10.1021/acsanm.9b02250
34. Lu, T.; Chen, F. Multiwfn: A multifunctional wavefunction analyzer. *J. Comput. Chem.* **2012**, *33*, 580– 592, DOI: 10.1002/jcc.22885
35. Gao, R.; Wang, K.; Wang, F.; Wang, H.; Wang, X.; Ren, J.; Wang, R. Synthetic perylenequinone as anchoring center of sulfur and catalyst for polysulfides conversion. *Chem. Eng. J.* **2023**, *455*, 140847, DOI: 10.1016/j.cej.2022.140847
36. Wang, L.; Guan, E.; Wang, Y.; Wang, L.; Gong, Z.; Cui, Y.; Meng, X.; Gates, B. C.; Xiao, F.-S. Silica accelerates the selective hydrogenation of CO_2 to methanol on cobalt catalysts. *Nat. Commun.* **2020**, *11*, 1033 DOI: 10.1038/s41467-020-14817-9
37. Fang, S.; Zhu, X.; Liu, X.; Gu, J.; Liu, W.; Wang, D.; Zhang, W.; Lin, Y.; Lu, J.; Wei, S.; Li, Y.; Yao, T. Uncovering near-free platinum single-atom dynamics during electrochemical hydrogen evolution reaction. *Nat. Commun.* **2020**, *11*, 1029 DOI: 10.1038/s41467-020-14848-2
38. Wei, S.; Zheng, P.; Xu, W.; Chen, S.; Xia, Y.; Cao, Y.; Zhu, K.; Cui, Q.; Wen, W.; Wu, C.; Wang, C.; Song, L. Operando exploring and modulating phase evolution chemistry from MAX to MXenes in molten salt synthesis. *J. Am. Chem. Soc.* **2023**, *145*, 10681– 10690, DOI: 10.1021/jacs.3c01083
39. Wangmo, S.; Song, R.; Wang, L.; Jin, W.; Ding, D.; Wang, Z.; Zhang, R.-Q. Strong interactions and charge transfers between a charged benzene molecule and multilayer graphenes. *J. Mater. Chem.* **2012**, *22*, 23380– 23386, DOI: 10.1039/c2jm35634a
40. Wang, Z.; Shen, J.; Ji, S.; Xu, X.; Zuo, S.; Liu, Z.; Zhang, D.; Hu, R.; Ouyang, L.; Liu, J.; Zhu, M. B, N Codoped graphitic nanotubes loaded with Co nanoparticles as superior sulfur host for advanced Li–S batteries. *Small* **2020**, *16*, 1906634, DOI: 10.1002/smll.201906634
41. Li, Y.; Fan, J.; Zhang, J.; Yang, J.; Yuan, R.; Chang, J.; Zheng, M.; Dong, Q. A honeycomb-like Co@N–C composite for ultrahigh sulfur loading Li–S batteries. *ACS Nano* **2017**, *11*, 11417– 11424, DOI: 10.1021/acsnano.7b06061
42. Hu, C.; Yang, C.; Yang, J.; Han, N.; Yuan, R.; Chen, Y.; Liu, H.; Xie, T.; Chen, R.; Zhou, H.; Liu, W.; Sun, X. An entangled cobalt–nitrogen–carbon nanotube array electrode with synergetic confinement and electrocatalysis of polysulfides for stable Li–S batteries. *ACS Appl. Energy Mater.* **2019**, *2*, 2904– 2912, DOI: 10.1021/acsaem.9b00243
43. Wang, Y.; Li, M.; Xu, L.; Tang, T.; Ali, Z.; Huang, X.; Hou, Y.; Zhang, S. Polar and conductive iron carbide@N-doped porous carbon nanosheets as a sulfur host for high performance lithium sulfur batteries. *Chem. Eng. J.* **2019**, *358*, 962– 968, DOI: 10.1016/j.cej.2018.10.086
44. Xiao, K.; Wang, J.; Chen, Z.; Qian, Y.; Liu, Z.; Zhang, L.; Chen, X.; Liu, J.; Fan, X.; Shen, Z. X. Improving polysulfides adsorption and redox kinetics by the Co_4N nanoparticle/N-doped carbon composites for lithium-sulfur batteries. *Small* **2019**, *15*, 1901454, DOI: 10.1002/smll.201901454
45. Rui, X. H.; Ding, N.; Liu, J.; Li, C.; Chen, C. H. Analysis of the chemical diffusion coefficient of lithium ions in $Li_3V_2(PO_4)_3$ cathode material. *Electrochim. Acta* **2010**, *55*, 2384– 2390, DOI: 10.1016/j.electacta.2009.11.096
46. Liu, F.-J.; Luo, W.-L.; Zhang, Z.; Yu, J.; Cai, J.-X.; Yang, Z.-Y. Cation-doped V_2O_5 microsphere as a bidirectional catalyst to activate sulfur redox reactions for lithium-sulfur batteries. *Chem. Eng. J.* **2023**, *456*, 140948 DOI: 10.1016/j.cej.2022.140948
47. Chu, R.; Nguyen, T.; Bai, Y.; Kim, N.; Lee, J. Uniformly controlled treble boundary using enriched adsorption sites and accelerated catalyst cathode for robust lithium-

sulfur batteries. *Adv. Energy Mater.* **2022**, *12*, 2102805, DOI: 10.1002/aenm.202102805
48. Wang, Z.; Liu, J.; Zhang, B. H.; Sun, L.; Cong, L.; Lu, L.; Mauger, A.; Julien, C. M.; Xie, H.; Sun, H. Modulating molecular orbital energy level of lithium polysulfide for high-rate and long-life lithium-sulfur batteries. *Energy Storage Mater.* **2020**, *24*, 373–378, DOI: 10.1016/j.ensm.2019.07.035
49. Yang, J.; Xiong, P.; Shi, Y.; Sun, P.; Wang, Z.; Chen, Z.; Xu, Y. Rational molecular design of benzoquinone-derived cathode materials for high-performance lithium-ion batteries. *Adv. Funct. Mater.* **2020**, *30*, 1909597 DOI: 10.1002/adfm.201909597
50. Xu, J.; Xu, L.; Zhang, Z.; Sun, B.; Jin, Y.; Jin, Q.; Liu, H.; Wang, G. Heterostructure ZnSe-$CoSe_2$ embedded with yolk-shell conductive dodecahedral as two-in-one hosts for cathode and anode protection of lithium-sulfur full batteries. *Energy Storage Mater.* **2022**, *47*, 223– 234, DOI: 10.1016/j.ensm.2022.02.010